

High Energy Absorption Nacre-Like Calcium Silicate Hydrate (C-S-H) Composite Toward Elastic Cementitious Materials

Xin Liu, Pan Feng,* Cristina Ruiz Agudo,* Huiwen Sun, Xiaohan Yu, Jonathan Avaro, Jiale Huang, Dongshuai Hou, Qianping Ran, Jinxiang Hong, Jiaping Liu, Changwen Miao, and Helmut Cölfen*

The low toughness under the tension of cement and concrete materials has been a long-standing issue for decades and it has become increasingly urgent to address in modern society due to the growing demand for the development of high-performance and sustainable constructions. Manipulating calcium silicate hydrate (C-S-H), the main hydration product of Portland cement, which determines the mechanical properties of cementitious materials, is an attractive method for improving their toughness following a bottom-up approach. Inspired by the microstructure of nacre, a high energy absorption C-S-H-based composite with a highly ordered structure is fabricated by a designed ternary building block, in which exfoliated montmorillonite provides a template for the nucleation and growth of C-S-H generating the “brick”, and polyvinyl alcohol acts as a “mortar” binding all the building blocks together. With the hierarchical toughening strategy explored here, the obtained C-S-H composite achieves a remarkable energy absorption of $16.2 \pm 2.6 \text{ MJ m}^{-3}$, which surprisingly outperforms the ultra-high toughness cementitious materials by a factor of 20–60 and is even higher than that of natural nacre and other nacre-like composites. These findings not only provide valuable insights into enhancing the toughness of cementitious materials but also open possibilities for broadening potential applications of C-S-H.

construction material and the second most consumed material worldwide after water, is one of the typical representatives of this conflict. The major limitation of concrete materials is the low toughness under tension, which is referred to as the inferior capability to absorb energy and plastically deform without fracturing. In particular, the tensile strength of concrete is less than one-tenth of its compressive strength, and the ultimate elongation is constrained to $\approx 10^{-4}$.^[2] As a result, concrete materials are highly susceptible to cracking under tensile stress due to their inherent brittleness, which severely threatens the durability of the concrete structure and thereby inflates the maintenance cost.

Extensive strategies have been proposed to enhance the toughness of cementitious binders, for example, reinforcement by steel rebar or different kinds of fibers,^[3] the addition of polymers^[4] together with modification by nanomaterials,^[5] among others. Although these toughening approaches improve the toughness of cement-based materials to some extent, the development

of super-high, -large, and -long-span infrastructures in modern society put forward a higher demand for enhanced toughness of cementitious materials.

1. Introduction

The conflict between strength and toughness has long been a persistent challenge in materials science.^[1] Concrete, the main

X. Liu, P. Feng, X. Yu, J. Huang, Q. Ran, J. Hong, J. Liu, C. Miao
Jiangsu Key Laboratory of Construction Materials
School of Materials Science and Engineering
Southeast University
Nanjing 211189, China
E-mail: pan.feng@seu.edu.cn

X. Liu, C. R. Agudo, H. Cölfen
Physical Chemistry
University of Konstanz
Universitätsstraße 10, 78457 Konstanz, Germany
E-mail: cristina.ruiz-agudo@uni-konstanz.de; helmut.coelfen@uni-konstanz.de
H. Sun, D. Hou
Department of Civil Engineering
Qingdao University of Technology
Qingdao 266033, China
J. Avaro
EMPA
Swiss Federal Laboratories for Materials Science and Technology
Lerchenfeldstrasse 5, St. Gallen CH-9014, Switzerland

The ORCID identification number(s) for the author(s) of this article can be found under <https://doi.org/10.1002/adfm.202307437>

© 2023 The Authors. Advanced Functional Materials published by Wiley-VCH GmbH. This is an open access article under the terms of the Creative Commons Attribution License, which permits use, distribution and reproduction in any medium, provided the original work is properly cited.

DOI: 10.1002/adfm.202307437

As the main component of hydrated cement paste, the calcium silicate hydrate (C-S-H) binding phase plays a pivotal role in concrete performance, affecting the mechanical properties, creep, shrinkage, and durability of the constructions.^[2] Therefore, C-S-H is widely regarded as the “gene” of cementitious materials where the mesoscopic disorder of amorphous C-S-H in cement systems may determine its brittleness and, by extension, the properties of concrete materials.^[6,7]

Manipulating the composition, structure, and performance of C-S-H from the bottom up has attracted great interest in recent years not only owing to its crucial role in cementitious materials but also its potential functional applications, such as bone tissue engineering,^[8] drug delivery,^[9] or energy storage.^[10] Some material scientists have explored ways to improve the toughness of C-S-H by controlling its porosity. A novel pathway involves producing micrometer cubic C-S-H particles with the aid of cetyltrimethylammonium bromide (CTAB), which decreases the porosity of C-S-H and leads to a significant improvement in toughness and ductility by $\approx 300\%$ and 77% higher than those of the control sample, respectively.^[11] Atomistic modeling and statistical analysis suggest that inducing the formation of nanovoids significantly increases the toughness and ductility of C-S-H owing to the combined mechanisms of crack deflection, void coalescence, internal necking, accommodation, and geometry of individual voids/particles.^[12]

Fabricating organic and inorganic composites has traditionally been an effective way to obtain tough materials and can be applied to cementitious systems. Molecular dynamic simulations indicate that polyethylene glycol (PEG) can considerably improve the ductility of C-S-H by the bridging effect of the polymer and the formation of Si—O—C bonds at the interface.^[13] More prominently, the ordered and layered inorganic–organic C-S-H mesocrystals over hundreds of micrometers are experimentally synthesized, exhibiting a bending strength of up to 153 MPa, mechanically analogous to nacre.^[14] In addition, nano-engineering has also brought some new insights into creating versatile high-performance nanostructures in which 2D materials, for example, graphene oxide (GO),^[15] silicene,^[16] and carrot-based cellulose nanosheets,^[17] could be promising candidates for designing tough C-S-H-based hybrids according to molecular dynamic simulations. By using GO as a restricting platform, researchers have experimentally controlled the ordered growth of C-S-H, resulting in 1–2 orders of magnitude improvement in strength compared to the disordered C-S-H.^[18]

From the literature above, most studies on C-S-H toughening focus on the simulation level. Although some successful cases have been experimentally achieved, they are generally restricted to small-length scales. To translate these innovative concepts into real-world applications, it is imperative to develop further a viable processing method that could be integrated into macroscopic structures at larger length scales. Nacre is a striking model from nature with remarkable strength and toughness due to the ingenious hierarchical structure and precisely designed interfaces.^[19] Various kinds of artificial nacre-like composite have been replicated by mimicking its architecture using creative methods such as freeze casting,^[20] layer-by-layer deposition,^[21] electrophoretic deposition,^[22] or mechanical assembly.^[23]

Inspired by the exquisite hierarchical structure of nacre, herein, we develop a highenergy absorption C-S-H composite

with highly ordered laminar microstructure by an upscaled and robust fabrication method. Our fabrication route involves producing a ternary building block in which exfoliated montmorillonite (MMT) (Figure S2, Supporting Information) with 2D characteristics is selected as a template for the nucleation and growth of C-S-H, and polyvinyl alcohol (PVA) serves as a “mortar” adsorbing onto the inorganic component. The unique nacre-like hierarchical structure enables the C-S-H composite to show a multiple cracking mode and strain hardening during the deformation under the tensile load. Surprisingly, the C-S-H composite’s energy absorption under tension can reach up to $16.2 \pm 2.6 \text{ MJ m}^{-3}$ due to the toughening mechanism from different length scales, which is ≈ 20 –60 times higher than that of the ultra-high toughness cementitious materials and even higher than that of other existing artificial nacre-like composites. Furthermore, the C-S-H composite presents efficient fire retardancy and improved durability. Our study not only opens more possibilities to improve the toughness of cementitious materials from the bottom up but also provides insights into novel potential applications of C-S-H.

2. Results and Discussion

The fabrication of the nacre-like C-S-H composite involves three steps, as depicted in **Figure 1a**. In the first step, C-S-H is synthesized by the double decomposition method in the presence of MMT. The exfoliated MMT possessing a 2D characteristic (Figure S3, Supporting Information) is a perfect template for the nucleation and growth of C-S-H. First, MMT shares resemblances with C-S-H in structure and chemical composition, showing a close affinity with C-S-H.^[24] Second, as an economical 2D material, MMT has been widely used in cementitious materials, showing good compatibility with cement.^[25] After the formation of C-S-H, in the second step, PVA is added, capable of adsorbing onto C-S-H through Ca coordination and hydrogen bonds,^[26] which glues all the building blocks together, forming a flexible network in the following step. At last, the homogeneous building blocks with a high aspect ratio tend to stack layer by layer under vacuum filtration, yielding a “brick and mortar” structure in which the inorganic component C-S-H/MMT functions as the “brick” and organic component PVA as the “mortar”.

The nucleation of C-S-H in the presence of MMT was investigated by in situ titration experiments, as shown in Figure 1b,c. In this set of experiments, supersaturation with respect to C-S-H was generated by the stepwise addition of calcium and silicate solutions to a water-container reservoir, with and without MMT, which eventually resulted in the precipitation of C-S-H. Upon C-S-H nucleation in solution, calcium, silicate, and hydroxide ions are consumed significantly, as displayed in Figure 1c, which leads to measurable changes in the pH, conductivity, free calcium, and transmittance of the solution. This allows us to determine the nucleation point independently by different probes. The time points corresponding to the abrupt alteration of these four parameters perfectly coincide (see Figure 1c; Figure S4, Supporting Information), and thus, we can assign them to C-S-H nucleation. From Figure 1b, it is concluded that MMT has a negligible effect on the pre-nucleation stage of C-S-H, where free calcium ions for both cases linearly increase at the same pace over time, that is the same slope in the free Ca curve in the pre-nucleation regime. Although the uptake of Ca by MMT may influence the free-Ca

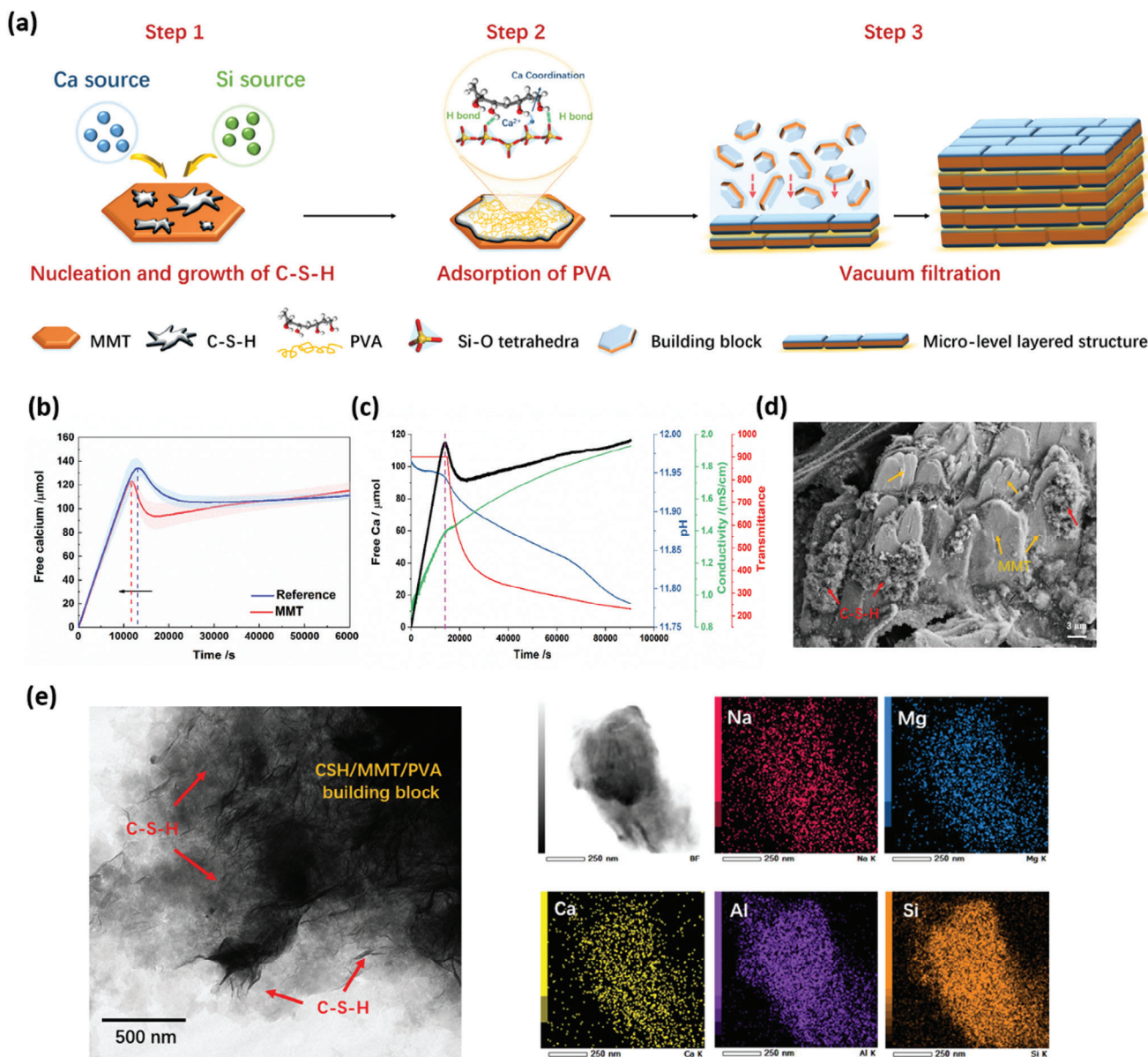


Figure 1. The fabrication scheme of the C-S-H composite and the nucleation behavior of C-S-H in the absence and presence of MMT. (a) Schematic diagram showing the procedure for fabricating the C-S-H composite. (b) Effects of MMT on the free calcium ions during the formation of C-S-H. (c) The evolution of free calcium ions, pH, conductivity, and transmittance with time while forming C-S-H in the presence of MMT. (d) The SEM image showing the nucleation of C-S-H on the surface of MMT at an early age. (e) The TEM image and EDS mappings of the CSH/MMT/PVA building block of C-S-H composites.

concentration in solution due to the cation exchange reaction,^[27] this effect is most likely very limited in this study and, thus, not measurable. However, MMT accelerates the nucleation of C-S-H, as evidenced by an earlier nucleation point of C-S-H shifting from 3.6 to 3.3 h. This could be due to the presence of extra MMT surfaces, which might provide sites for the heterogeneous nucleation of C-S-H, lowering the energy barrier required for its formation. The precipitation of C-S-H in the titration experiments in the presence and absence of MMT was confirmed by XRD (Figure S5, Supporting Information).

Figure 1d provides additional evidence to explain the facilitation of C-S-H nucleation by MMT. At an early age, C-S-H with the typical flocculent morphology is found to nucleate on the smooth MMT surface, most likely due to a seeding effect.^[28] Figure 1e shows the morphology and element composition of the CSH/MMT/PVA building block after 3 days of reaction with PVA. We observe from Figure 1e that the foil-like C-S-H sheets precipitated on the surface of MMT, especially near the edge. The formation of C-S-H, along with the adsorption of PVA, most likely wraps MMT and thereby increases the particle size,

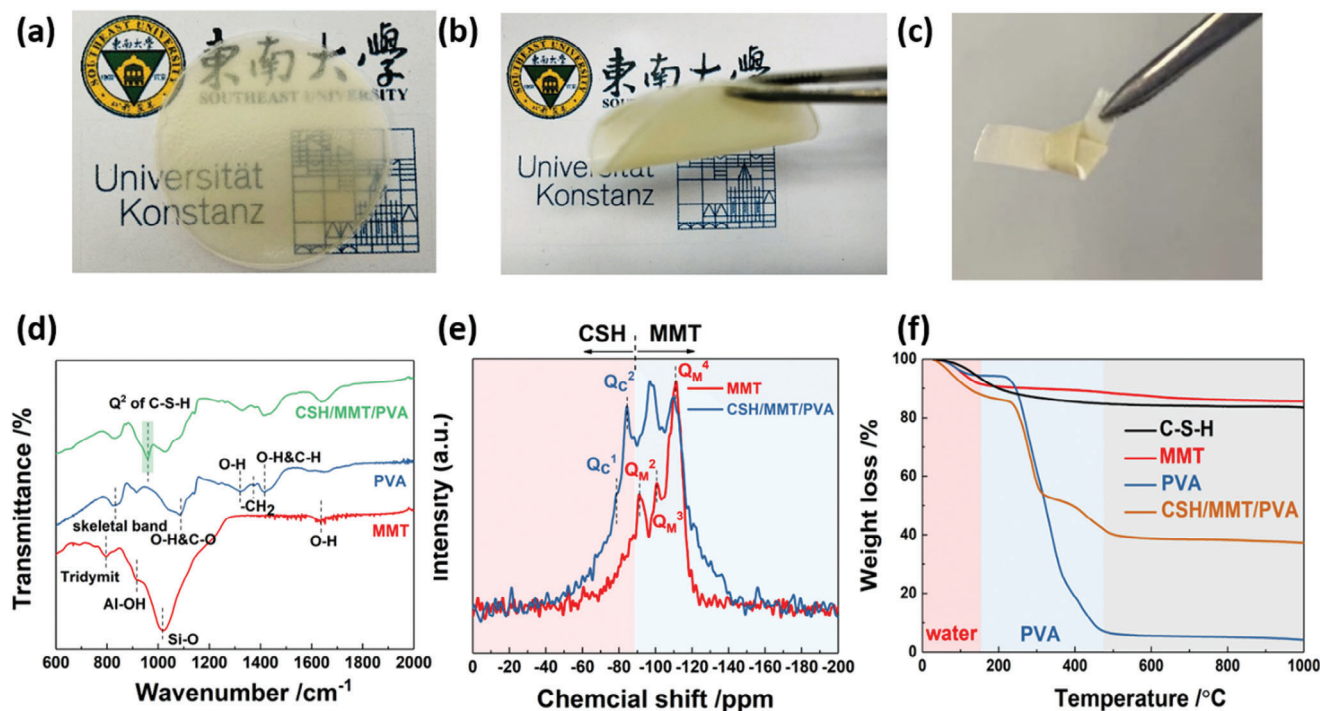


Figure 2. The free-standing C-S-H composite and its composition. (a) Optical photograph of the fabricated free-standing C-S-H composite, which shows a certain transparency. (b) Optical photograph of bent C-S-H composite showing excellent bending strength. (c) Optical photograph of knotted C-S-H composite strip. (d) The FTIR spectra of MMT, PVA, and C-S-H composite. (e) NMR spectra of MMT and C-S-H composite. (f) The TGA curve of C-S-H, MMT, PVA, and C-S-H composite.

shifting the size distribution to a larger range (Figure S6, Supporting Information). The reduced total organic content (TOC) after the synthesis further gives a clue on the adsorption of PVA on the building block (Table S1, Supporting Information). Notably, in the presence of MMT, the crumples due to the out-of-plane deformation of C-S-H are not pronounced as those without MMT (Figure S7, Supporting Information). The confinement of 2D MMT might guide C-S-H toward in-plane growth, thus mitigating the defectives caused by the disordered growth.^[18] EDS mappings demonstrate that Na, Mg, Si, Ca, and Al, the primary characteristic elements, are evenly distributed on the surface of the building block (Figure 1e). The detection of Ca and its homogeneous distribution on the building block further verifies the formation of C-S-H on the surface of MMT.

A free-standing composite is obtained upon peeling from the filtration membrane, as shown by the optical photograph in Figure 2a. The composite exhibits a certain degree of transparency partially due to the reduction in light scattering within the well-aligned microstructure, as introduced in the following content.^[29] The slightly yellowish color of the composite originates from MMT (Figure 2a). In addition, the composite can be effortlessly bent (Figure 2b) and even knotted (Figure 2c) without any crack, displaying exceptional flexibility.

FTIR and NMR were carried out in the current study to reveal the formation of C-S-H in the composite. As shown in Figure 2d, the characteristic bands of PVA are observed at the wavenumbers of ≈ 828 , 1086, 1318, and 1415 cm⁻¹, which are attributed to PVA skeletal band, in-plane deformation of O—H and stretching of C—O, in-plane deformation of O—H with CH wagging and in-

plane deformation of O—H and C—H, respectively.^[30] In the composite spectrum, we also observe the fingerprint band of MMT at 1016 cm⁻¹ ascribed to Si—O—Si stretching.^[31] On top of that, a new band at 960 cm⁻¹ appears, which is attributed to the Si—O stretching of Q² tetrahedra in C-S-H.^[32] The band at ≈ 1642 cm⁻¹ related to H—O—H bending vibration increases, further suggesting the formation of C-S-H given the presence of H₂O in C-S-H.^[32]

Moreover, ²⁹Si NMR results provide more clues for the formation of C-S-H in the composite, as shown in Figure 2e. The signal at the chemical shift of -111 ppm corresponding to Q⁴ in MMT is retained after forming the composite.^[33] The signals at chemical shifts of -101 and -92 ppm attributed to Q³ and Q² in MMT, respectively,^[33] merge into one signal in the composite at the chemical shift of -97 ppm, being not explicitly separated by ²⁹Si NMR. A remarkable new signal is found in the composite at the chemical shift of -85 ppm, ascribed to Q² in C-S-H.^[34] Additionally, a bump signal at -79 ppm is detected in the composite corresponding to Q¹ in C-S-H.^[34] Based on EDS, FTIR, and ²⁹Si NMR results, we conclude the successful formation of C-S-H in the composite.

TGA was used to determine the content of the organic component in the system. As shown in Figure 2f, three steps are involved in the decomposition of the C-S-H composite from 30 to 1000 °C. In the first step, the C-S-H composite undergoes a continuous weight loss from 30 to 150 °C, which can be attributed to the physically bound water in the sample. The dramatic decomposition of PVA usually occurs at 240–490 °C, as seen in Figure 2f. By this, we estimate the content of PVA

in the C-S-H composite is $\approx 45\%$ according to the tangential method (Figure S8a, Supporting Information). Given the partial temperature overlapping of PVA decomposition and the continuous weight loss of C-S-H and MMT, the PVA content might be slightly overestimated in this study. The weighting method is implemented to evaluate the content of C-S-H and MMT due to the absence of their characteristic decomposition temperature in the TGA curve, by which the inorganic component consists of $\approx 70.5\%$ C-S-H and 29.5% MMT (Figure S8b, Supporting Information). Thus, the combination of TGA and weighting method indicates the C-S-H composite is composed of $\approx 45\%$ PVA, 39% C-S-H, and 16% MMT.

The microstructure of the cross-section of the C-S-H composite was examined by SEM, as shown in Figure 3a. Similar to nacre, the building blocks of the C-S-H composite are stacked layer by layer, resulting in an extremely dense and highly aligned lamellar structure. This microstructural feature was further confirmed by bench-top grazing-incidence small-angle scattering (GISAS) measurements. Our results demonstrated the presence of a scattering peak at 1.5 nm , associated with the mineral thickness, which presented a high degree of alignment parallel to the substrate and characterized by Herman's orientation factor of 0.65 (Figure S9 and Table S2, Supporting Information). The nitrogen sorption measurement suggests a nonporous structure due to the absence of N_2 adsorption onto the sample, as indicated by the negative adsorption quantity (Figure S10, Supporting Information). The magnified SEM image in Figure 3a shows that the layer of the C-S-H composite presents a unique waviness rather than flatness. This feature seems to play a crucial role in enhancing the energy absorption ability of the C-S-H composite, which will be discussed in the following. In line with TEM-EDS, the SEM-EDS element mapping results suggest a uniform element distribution (Figure 3b).

Due to the extraordinary bending strain shown by Figure 2b-c, uniaxial tensile measurements offer the appropriate method to assess the mechanical properties of the C-S-H composite quantitatively, consistent with the other film-like sample characterizations.^[35,36] For that, dog bone-like samples were fabricated, as shown by the inset in Figure 3c, to ensure robust mechanical properties. The typical stress and strain curves of the C-S-H composite are depicted in Figure 3d, which show that the C-S-H composite exhibits a linear elastic deformation at low strain ranges, followed by a broad region of large plastic deformation, that is, strain hardening, before fracture. Commonly existing axial misalignment during the tensile strength measurement readily leads to the deviation of the individual measurements, as shown in Figure 3c, and thus, the averaged mechanical parameters are reported in this study. The average tensile strength calculated was $15.8 \pm 2.1\text{ MPa}$, with the tensile strain capable of reaching up to $125.3 \pm 19.7\%$, giving rise to an impressive energy absorption under tension of $16.2 \pm 2.6\text{ MJ m}^{-3}$ (Table S3, Supporting Information). Such high energy absorption is substantially higher than ordinary Portland cement-based materials and is $\approx 20\text{--}60$ times higher than ultra-high toughness cementitious materials (UHTCC) reinforced by fibers, which are also known as engineered cementitious materials (ECC) or strain-hardening cementitious materials (SHCC).^[37] Compared with natural nacre, the energy absorption of the C-S-H composite presented here is improved by a factor of $10\text{--}100$. Moreover, the energy absorption

of the C-S-H composite also outperforms that of other artificial nacre-like composites, for example, MMT-based nacre-like composite and graphene oxide (GO) based nacre-like composite, as depicted in the Ashby plot in Figure 3g and Table S4 (Supporting Information).

A closer observation of the stress-strain curve of the C-S-H composite (Figure 3d) suggests two scenarios might be included in the strain-hardening region, given the slight change of the slope. In Region II, multiple parallel crackings were visible on the surface of the C-S-H composite, as displayed in Figure 3e, which is likely derived from the extensive sliding of the platelets.^[38] After the fracture of the C-S-H composite, we observed the well-aligned failed polymer on the cross-section of the C-S-H composite, as indicated by the arrows in Figure 3f, which could have resulted from the compression of adjacent ordered inorganic platelets that led to the rearrangement of polymer chains in between along the loading direction applied (Figure 4). Furthermore, compared with Figure 3a, the cross-section of the fractured composite shows a more irregular morphology, indicating that the platelet pull-out instead of platelet fracture is the dominating fracture mode.^[39] Based on these results, we propose a trilinear model to simplify the mechanical response of the C-S-H composite under tensile stress. In region I, the C-S-H composite undergoes a linear elastic deformation without cracking. In Region II, the increase of strain leads to the formation of multiple cracks. In Region III, the further increase of strain transfers the load to the polymer network in the C-S-H composite, eventually leading to the pull-out and failure of the polymer.

Molecular dynamic (MD) simulations revealed the molecular-level interaction between C-S-H and MMT. From Figure 3h, the stress-strain curve obtained from the simulated uniaxial tension along the z -direction shows the failure of pure C-S-H at the strain of 0.20 \AA/\AA , while the CSH/MMT composite does not fail until the strain reaches 0.3 \AA/\AA . Notably, the stress of the CSH/MMT composite was found to be enhanced by 34% compared to the pure C-S-H. These simulation results, in accordance with our experimental findings, indicate the enhanced energy absorption of C-S-H by introducing MMT. A careful observation of the morphology change under the tension loading revealed the formation of a Ca-O_m (oxygen atom from MMT) bond at the interface between C-S-H and MMT, as suggested by the radial distribution function (RDF) peak of Ca-O_m located at 2.5 \AA (Figure S11a, Supporting Information), which bridges the adjacent C-S-H substrates impeding its fracture and thus improving the energy absorption ability of the composite. Despite the absence of any new chemical bonds apart from Ca-O_m , time correlation function (TCF) calculation unravels the presence of MMT in C-S-H, strengthens the stability of hydrogen bonds and $\text{O}_{\text{Si}}\text{--H}_w$ as indicated by the higher TCF values in CSH/MMT composite (Figure S11, Supporting Information).^[15] The increased stability of these chemical bonds is also likely to contribute to the overall improvement in the energy absorption of the CSH/MMT composite.

Based on all the results discussed above, the synergetic contributions of C-S-H, MMT, and PVA at various hierarchical levels are considered the underlying reason for achieving the exceptionally high energy absorption of the C-S-H composite, as shown in Figure 4. At the molecular level, the intensive literature reports that energy dissipation during deformation occurs

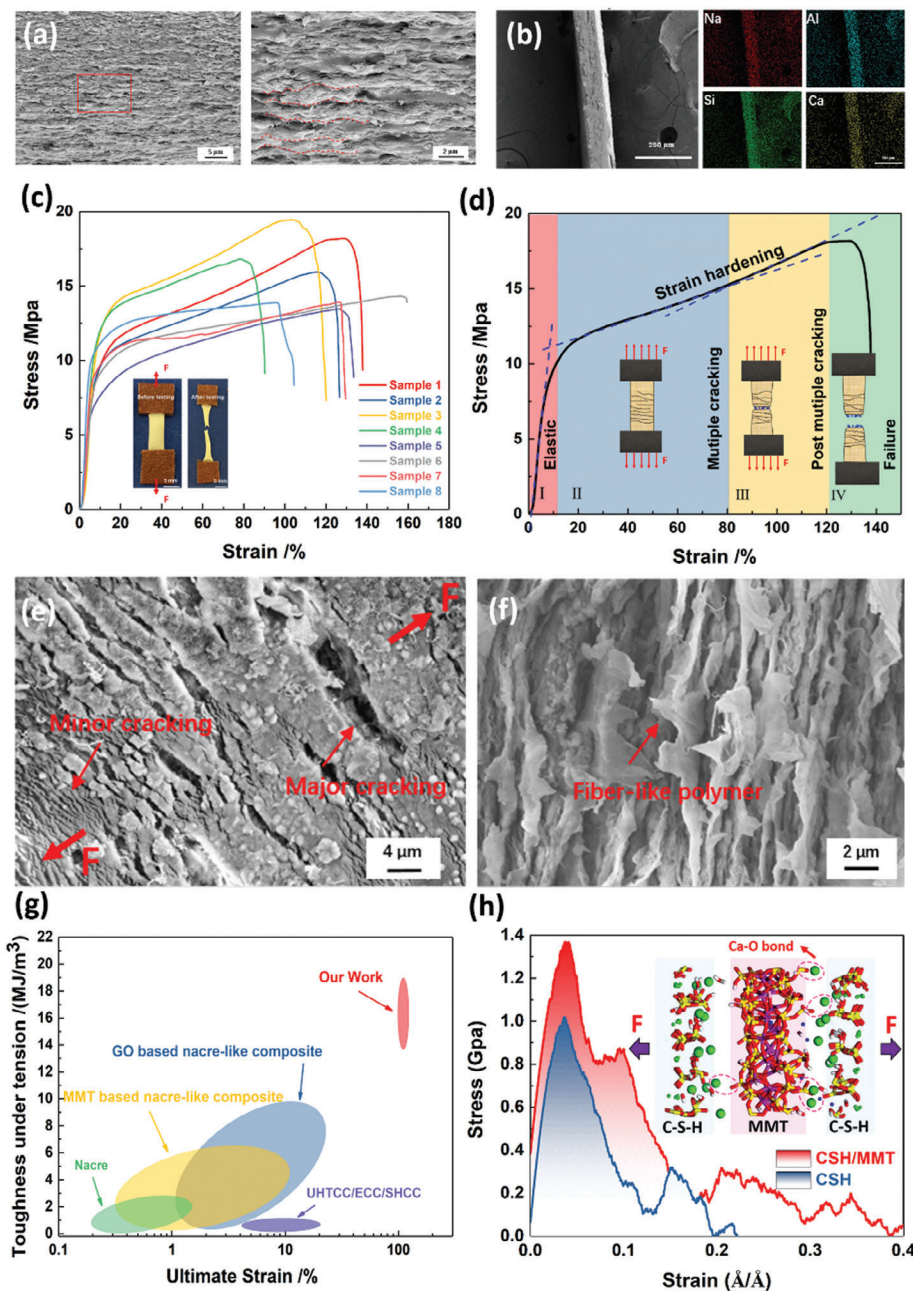


Figure 3. The microstructure and mechanical properties of the C-S-H composite. (a) SEM image of the cross-section of C-S-H composite showing a highly ordered laminar structure. (b) Cross-section of the C-S-H composite and EDS mappings. (c) The stress-strain curve of the C-S-H composite. The inset shows the specimen before and after the tensile strength measurement. (d) A typical deformation behavior of the C-S-H composite. (e) The multiple cracking modes on the surface of the C-S-H composite before fracture. (f) The SEM image of the cross-section of the C-S-H composite after fracture. (g) The Ashby plot displays the energy absorption under tension against the strain of different comparable natural and artificial materials. (h) Simulated stress-strain curve of the C-S-H and CSH/MMT composite. The inset depicts the snapshot of the CSH/MMT composite at the strain of around 0.05 Å/Å in which Ca—O_m bonds are formed at the interface of MMT and C-S-H.

by unfolding domains and breaking cross-links in the polymer's molecular chain.^[40,41] On top of that, our MD simulations imply that the formation of stable Ca—O_m bonds at the C-S-H and MMT interface, together with the enhanced stability of hydrogen bonds and Osi-Hw—O_w bonds by MMT, reinforces the mechanical properties of the CSH/MMT composite. At the nanoscale, the viscoelastic nature of the polymer and the presence of nanoasper-

ities are thought to be the two dominant toughening mechanisms in the nacre.^[38,42] Likewise, in the C-S-H composite presented in the current study, the folded PVA network adhered to the inorganic component bridges the adjacent platelets, enabling it to endure substantial stretches under loading. This would result in a significant viscoplastic deformation and thus dissipate energy, as evidenced by the fractured cross-section of the C-S-

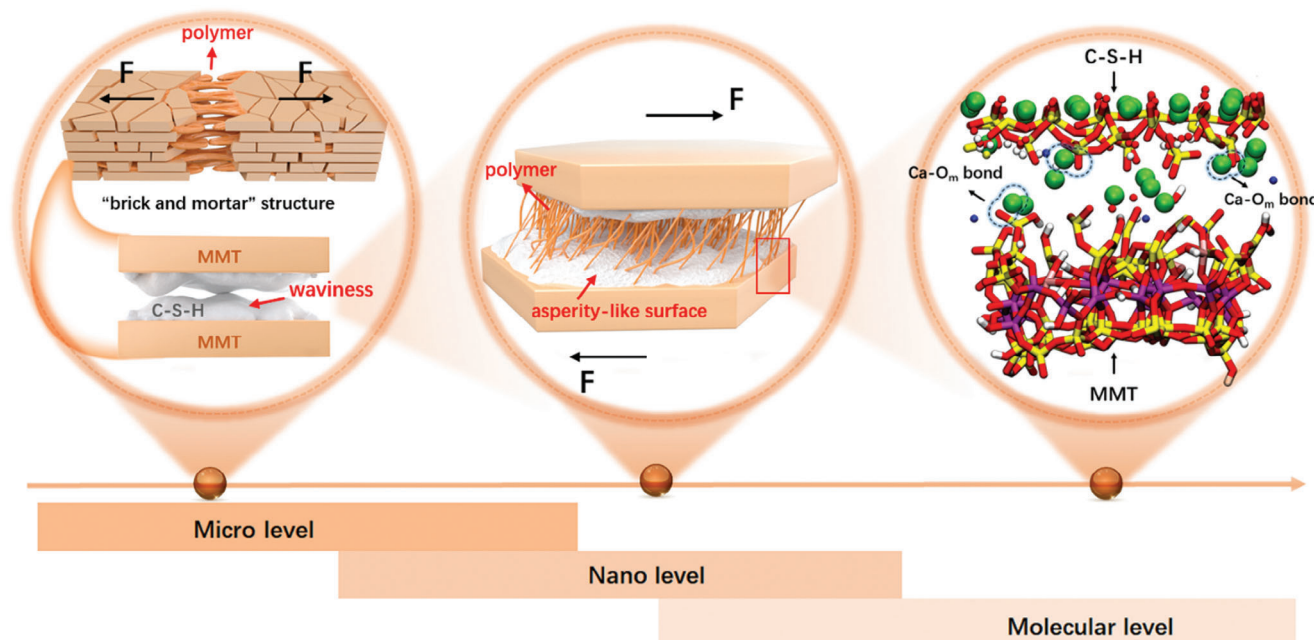


Figure 4. The hierarchical toughening mechanism of C-S-H composites.

H composite in Figure 3f. Moreover, C-S-H with a rough morphology grown onto MMT provides an asperity-like surface, as shown in Figure 1d, which enhances the interlocking effect via contact friction during sliding, further improving the energy absorption ability. At the micro level, as exhibited by the rugged surface of the fractured cross-section (see Figure 3f), platelet pull-out serves as the primary failure mode, which is responsible for the microcrack accumulation and crack deflection within a laminar structure.^[39,43] Furthermore, it is essential to highlight that introducing rough C-S-H produces a wavy tablet texture rather than a flat one, as seen in Figure 3a. According to simulations, this microstructural feature is regarded to be able to generate a progressive tablet interlocking and propagation of the inelastic deformation, that is, strain hardening,^[44] which significantly contributes to the overall energy absorption of the C-S-H composite in this study.

In addition to the superior mechanical properties, the C-S-H composite shows high efficiency in fire retardancy. When exposed to a flame, the C-S-H composite burns and turns black due to the burning of the polymer (**Figure 5a**). Once the polymer in the C-S-H composite is consumed, the remaining inorganic component would not support further combustion. During the burning, no plastic-like dripping of the hot liquid is found, and the shape of the C-S-H composite stays intact. It is important to note that the layered structure of the C-S-H composite is retained after burning, although the microstructure becomes less dense, most likely due to the burning of the polymer, as shown in Figure 5b.

Ca leaching is one of the indicators to evaluate the durability of C-S-H under a harsh environment, for example, sulfate attack, magnesium attack, carbonation, etc.^[45–47] The decalcification behavior of the C-S-H composite was investigated by the batch reaction in Milli-Q water under stirring, where the release of normalized calcium concentration over time is compared to the synthetic C-S-H (Figure S12, Supporting Information), as shown in

Figure 5c. Synthetic C-S-H shows a rapid increase in calcium ion concentration upon immersion in the solution, reaching the plateau within 50 min. Conversely, the C-S-H composite exhibits a slow release of calcium ions, with no plateau level even after 300 min. After 300 min leaching, the calcium ions of synthetic C-S-H are 13 times higher than that of the C-S-H composite, suggesting a considerably high resistance to decalcification. These results highlight the improved durability of the C-S-H composite, which can be attributed to its highly ordered and dense C-S-H structure.

The exceptional mechanical properties, efficient resistance to high temperature, and chemical stability endow the C-S-H composite with the potential for various applications, such as coating materials, refractories, and food packages not limited to cementitious materials.

3. Conclusion

In summary, inspired by nacre, a C-S-H-based composite with an exceptionally high energyabsorption ability has been fabricated using a scalable and robust strategy. The highly ordered hierarchical microstructure contributes to its excellent mechanical properties in which MMT provides a template for the precipitation of C-S-H, and PVA glues those inorganic building blocks, generating an adhesive network. With the finely designed brick-and-mortar structure, the energy absorption of the resultant C-S-H composite reaches up to $16.2 \pm 2.6 \text{ MJ m}^{-3}$, surpassing fiber-reinforced UHTCC by 20–60 times. In addition to the superior mechanical properties, C-S-H-based composite presents efficient fire retardancy and stability.

The results presented in our study underscore that controlling the growth of C-S-H into a highly ordered microstructure provides a promising strategy to enhance the toughness of cementitious materials from the bottom up. What is more important,

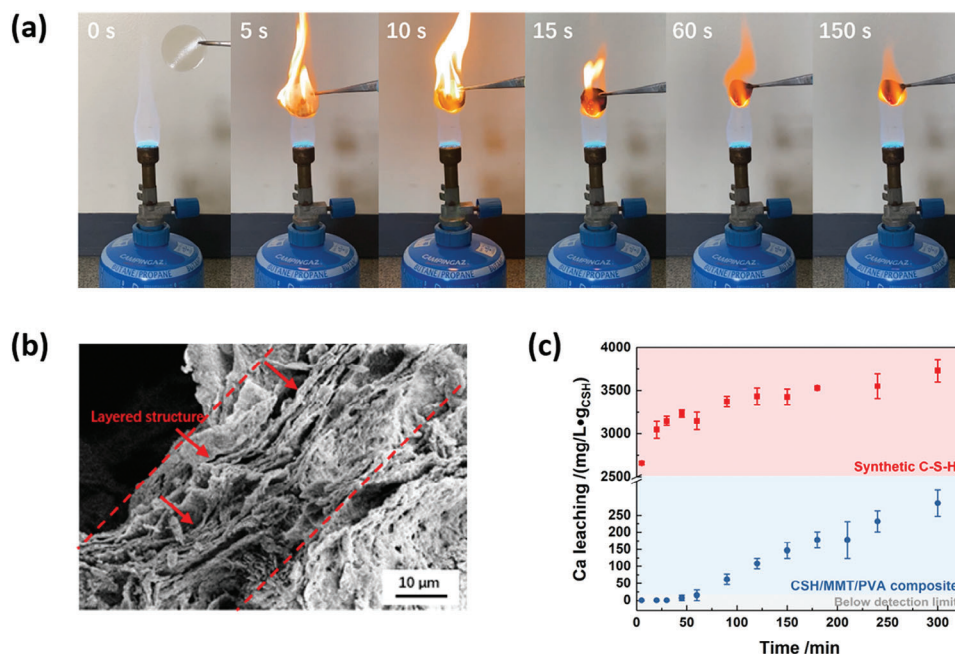


Figure 5. The fire retardancy and durability of C-S-H composite. (a) Optical photograph showing the change of the C-S-H composite subjected to blast burner. (b) The cross-section of the C-S-H composite after burning shows that the layered structure is maintained. (c) The Ca leaching of synthetic C-S-H and C-S-H composite with time.

the same strategy may be extended to other cement hydration products and thus contribute more to the overall toughness of cement and concrete. This could be realized with the aid of existing technologies for concrete production and the use of polymer and larger 2D materials, as reported in this study. The existing technologies include methods such as vacuum dewatering, spraying, magnetically controlling, and mechanical pressing methods, each of which might help improve the ordered alignment of materials at a wide range of length scales, covering, for instance, hydration products, fibers, and template materials.

4. Experimental Section

Materials: Sodium metasilicate nonahydrate ($\text{Na}_2\text{SiO}_3 \cdot 9\text{H}_2\text{O}$), MMT (K 30), and PVA ($M_w = 89\,000\text{--}98\,000\text{ g mol}^{-1}$) were purchased from Sigma-Aldrich. Calcium chloride (CaCl_2) and sodium hydroxide (NaOH) were obtained from Carl Roth GmbH (Karlsruhe, Germany). The ultrapure water (resistivity = $18.2\text{ M}\Omega\text{ cm}$) collected from Milli-Q direct water purification system (Merck) was used throughout. All the chemicals were used as received unless noted otherwise.

Exfoliation of MMT: MMT solution (0.5 wt.%) was prepared as the starting solution, which was intensively stirred by a magnetic stirrer at 800 rpm for 1 week, followed by standing for 24 h. The resulting supernatant was then subjected to an ultrasound bath for 6 h. Afterward, the solution was left to stand for another 24 h, and the supernatant was collected as the exfoliated MMT solution for the synthesis of the C-S-H composite in this study (Figure S1, Supporting Information).

Preparation of C-S-H Composite: The double decomposition method was used to synthesize C-S-H in the presence of MMT. In this method, Na_2SiO_3 solution (50 mL, 10 mmol L^{-1}) was added into 300 mL exfoliated MMT solution with the pH adjusted to 13 by NaOH solution (10 mol L^{-1}). Subsequently, CaCl_2 solution (50 mL, 10 mmol L^{-1}) was dropwise pumped into the above solution at the rate of 1.5 mL min^{-1} , while stirring for 3 h at 600 rpm. PVA solution (250 mL, 40 mg L^{-1}) prepared by heating at

$80\text{ }^\circ\text{C}$ was then added to the mixture. After 3 days of continuous stirring at 600 rpm, the solid was separated from the solution by centrifugation at 9000 rpm for 4 min and rinsed with Milli-Q water four times to remove the unabsorbed PVA and residual ions. Twenty five milliliters of Milli-Q water was added to the obtained gel-like solid and then subjected to the ultrasonic bath for 2 h (80 W) to achieve a homogeneous building block solution. Then, the solution was vacuum filtered using a polycarbonate membrane ($5\text{ }\mu\text{m}$, Isopore) to obtain a free-standing C-S-H composite after $\approx 12\text{ h}$. The optimization of the proportions for synthesizing the C-S-H composite is given in Figure S13 (Supporting Information).

Nucleation and Growth: The nucleation and growth behavior of C-S-H in the absence and presence of MMT was investigated by an in situ commercial titration system (Metrohm, Germany). For the case without MMT, a homemade Teflon beaker was filled with 100 mL Milli-Q water, whose pH was adjusted to 12 by NaOH solution as the base solution. Regarding the case with MMT, 100 mL base solution was taken from the mixture of 150 mL exfoliated MMT solution and 250 mL Milli-Q water, with its pH adjusted to 12. In both cases, CaCl_2 (40 mmol L^{-1}) and NaSiO_3 solution (40 mmol L^{-1}) were added simultaneously into the base solution at the dosing rate of 0.02 mL min^{-1} while stirring at 700 rpm. The pH, calcium potential, conductivity, and transmittance of the solution were monitored concurrently. Three replicates were carried out for each case to get the average and deviation values. The entire process was conducted in a glove box filled with N_2 to eliminate the contamination of CO_2 from the air.

Characterization: Scanning electron microscopy (SEM) was performed on a Zeiss Gemini 500 equipped with energy dispersive spectroscopy (EDS). The samples were coated with a layer of Au before observation. The images were collected at the acceleration voltage of 8 kV. A JEOL JEM-2200FS high-resolution transmission electron microscope (HRTEM) operated at 200 kV was used to observe the morphologies of samples. The diluted solution was dropped onto a copper grid and allowed to dry naturally under an ambient environment. An Agilent Cary 639 benchtop Fourier transform infrared spectroscopy (FTIR) with a resolution of 4 cm^{-1} was used to reveal the phase composition of the samples. The silicon environment of the samples was characterized by a Bruker Avance III 400 solid-state nuclear magnetic resonance (NMR). The spectra were

collected at the spinning speed of 10 kHz, relaxation delay of 60 s, scanning number of 4096, and a single pulse width of 5 μ s. Thermal gravimetric analysis (TGA) was conducted on a NETZSCH STA 499 F3 analyzer under an N_2 atmosphere, with a heating rate of 10 $^{\circ}C\ min^{-1}$ and a temperature range of 30–1000 $^{\circ}C$.

Mechanical Properties Measurement: C-S-H composite was cut into strips with a length of 25 mm and a width of 5 mm before measurements. All the strips were cut randomly in the x-y plane with no particular direction. Sandpaper with a grade number of 80 was firmly attached to both ends of the strip to prevent its slippage from the clamps during the loading. The tests were performed at room temperature and relative humidity of 30% on a Zwick Z005/1446 Retroline tC instrument using a gauge length of ≈ 12 mm and a loading rate of 10 mm min^{-1} .^[35,36] The thickness of each strip was measured by a torque digital micrometer before measurements. The mean mechanical parameters and deviation were evaluated from at least 12 individual measurements. The energy absorption under tension was calculated by integrating the stress–strain curve.

Molecular Dynamic (MD) Simulation: The tobermorite (22.32 $\text{\AA} \times 27.17 \text{\AA} \times 45.54 \text{\AA}$) and MMT super-cell model (20.72 $\text{\AA} \times 17.96 \text{\AA} \times 15 \text{\AA}$) used in this study were derived from 11 \AA tobermorite unit cell proposed by Hamid^[48] (Figure S14a, Supporting Information) and MMT unit cell proposed by Viani et al.^[49] (Figure S14b, Supporting Information), respectively. The CSH/MMT composite model (Figure S14d, Supporting Information) was created by inserting MMT within the interlayer region of the C-S-H matrix. As a comparison, a C-S-H gel model filled with water molecules at the two C-S-H substrates was constructed (Figure S14e, Supporting Information). The reaction force field MD simulation was performed in the LAMMPS package^[50] employing the ReaxFF force field. Initially, the interaction between C-S-H and MMT was calculated in the NPT ensemble at 300 K and 1 atm for 1 ns, with a step size of 0.25 fs. Subsequently, upon reaching the equilibrium, the uniaxial tensile simulation along the Z-axis was carried out under the NVT ensemble with a strain rate of 0.00008 ps^{-1} and a simulation time of 1 ns.

Fire Retardancy Measurement: The fire retardancy of the C-S-H composite was tested by a blast burner. A video recorded the whole process.

Durability Measurement: Synthetic C-S-H was prepared as a reference by adding $CaCl_2$ solution (500 mL, 0.1 mol L^{-1}) into Na_2SiO_3 solution (500 mL, 0.1 mol L^{-1}) at 5 mL min^{-1} while stirring at 600 rpm. After 3 days of stirring under a continuous flow of N_2 at room temperature, the C-S-H solid was obtained by vacuum filtration and then vacuum dried at 40 $^{\circ}C$ until constant weight. For Ca leaching measurement, 0.1 g synthetic C-S-H and C-S-H composite cut into small pieces were added into 100 mL Milli-Q water, respectively, and followed by stirring at 500 rpm. At specific time intervals, 0.2 mL solution was collected and then passed through a 0.2 μ m filter. The filtered solution was diluted by 1% HNO_3 solution for the determination of the Ca concentration by Agilent 5800 inductively coupled plasma-optical emission spectrometer (ICP-OES). The equipment was calibrated by 0.1, 1, and 5 mmol L^{-1} standard solution before measurements.

Supporting Information

Supporting Information is available from the Wiley Online Library or from the author.

Acknowledgements

This work was financially supported by the National Natural Science Foundation of China (nos. 51890904, 52122802, and 52078126), the Jiangsu Provincial Department of Science and Technology Innovation Support Program (nos. BK20222004 and BZ2022036), Shandong Provincial Education Department (no. 2019KJG010), and Taishan Scholars Program of Shandong Province (no. tsqn201812090). X.L. thanks the financial support from the China Scholarship Council (202106090089). C.R.A. thanks the Zukunftskolleg of the University of Konstanz for financial support. The authors would like to thank Dr. Hipassia M. Moura for the NMR measurements, and Dr. Bing Ni and Mr. Jian Zhou for the TEM measurements.

Open access funding enabled and organized by Projekt DEAL.

Conflict of Interest

The authors declare no conflict of interest.

Data Availability Statement

The data that support the findings of this study are available from the corresponding author upon reasonable request.

Keywords

calcium silicate hydrate (C-S-H), cement, energy absorption, montmorillonite, nacre inspired

Received: June 29, 2023
Revised: October 17, 2023
Published online: October 30, 2023

- [1] R. O. Ritchie, *Nat. Mater.* **2011**, 10, 817.
- [2] P. K. Mehta, P. J. M. Monteiro, in *Concrete: Microstructure, Properties and Materials*, McGraw-Hill, New York, USA **2017**.
- [3] V. Afrougsabet, L. Biolzi, T. Ozbakkaloglu, *J. Mater. Sci.* **2016**, 51, 6517.
- [4] R. Wang, P.-M. Wang, X.-G. Li, *Cem. Concr. Res.* **2005**, 35, 900.
- [5] J. Liu, J. Fu, T. Ni, Y. Yang, *Constr. Build. Mater.* **2019**, 200, 530.
- [6] K. Ioannidou, M. Kanduc, L. Li, D. Frenkel, J. Dobnikar, E. Del Gado, *Nat. Commun.* **2016**, 7, 12106.
- [7] K. Ioannidou, K. J. Krakowiak, M. Bauchy, C. G. Hoover, E. Masoero, S. Yip, F.-J. Ulm, P. Levitz, R. J.-M. Pellenq, E. Del Gado, *Proc. Natl. Acad. Sci. U. S. A.* **2016**, 113, 2029.
- [8] S. Ni, J. Chang, L. Chou, *J. Biomed. Mater. Res. A* **2006**, 76A, 196.
- [9] J. Wu, Y.-J. Zhu, S.-W. Cao, F. Chen, *Adv. Mater.* **2010**, 22, 749.
- [10] E. Shamsaei, F. Basquiroto De Souza, A. Fouladi, K. Sagoe-Crentsil, W. Duan, *ACS Appl. Energy Mater.* **2022**, 5, 958.
- [11] S. E. Moghaddam, V. Hejazi, S. H. Hwang, S. Sreenivasan, J. Miller, B. Shi, S. Zhao, I. Rusakova, A. R. Alizadeh, K. H. Whitmire, R. Shahsavari, *J. Mater. Chem.* **2017**, 5, 3798.
- [12] N. Zhang, R. Shahsavari, *J. Mech. Phys. Solids* **2016**, 96, 204.
- [13] Y. Zhou, D. Hou, G. Geng, P. Feng, J. Yu, J. Jiang, *Phys. Chem. Chem. Phys.* **2018**, 20, 8247.
- [14] A. Picker, L. Nicoleau, Z. Burghard, J. Bill, I. Zlotnikov, C. Labbez, A. Nonat, H. Cölfen, *Sci. Adv.* **2017**, 3, e1701216.
- [15] D. Hou, Z. Lu, X. Li, H. Ma, Z. Li, *Carbon* **2017**, 115, 188.
- [16] Q. Zheng, J. Jiang, C. Chen, J. Yu, X. Li, L. Tang, S. Li, *ACS Appl. Mater. Interfaces* **2020**, 12, 17806.
- [17] Y. Chi, B. Huang, M. Saafi, J. Ye, C. Lambert, *Composites, Part B* **2020**, 199, 108235.
- [18] F. Basquiroto De Souza, E. Shamsaei, S. Chen, K. Sagoe-Crentsil, W. Duan, *Commun. Mater.* **2021**, 2, 84.
- [19] J. Wang, Q. Cheng, Z. Tang, *Chem. Soc. Rev.* **2012**, 41, 1111.
- [20] K. Yin, B. A. Reese, C. R. Sullivan, U. G. K. Wegst, *Adv. Funct. Mater.* **2020**, 31, 2007743.
- [21] Q. Chen, Z. Ma, Z. Wang, L. Liu, M. Zhu, W. Lei, P. Song, *Adv. Funct. Mater.* **2021**, 32, 2110782.
- [22] C.-A. Wang, B. Long, W. Lin, Y. Huang, J. Sun, *J. Mater. Res.* **2008**, 23, 1706.
- [23] M. Morits, T. Verho, J. Sorvari, V. Liljeström, M. A. Kostianen, A. H. Gröschel, O. Ikkala, *Adv. Funct. Mater.* **2017**, 27, 1605378.

- [24] R. Zhu, Q. Chen, Q. Zhou, Y. Xi, J. Zhu, H. He, *Appl. Clay Sci.* **2016**, 123, 239.
- [25] T.-P. Chang, J.-Y. Shih, K.-M. Yang, T.-C. Hsiao, *J. Mater. Sci.* **2007**, 42, 7478.
- [26] Y. Zhou, L. Tang, J. Liu, C. Miao, *Cem. Concr. Res.* **2019**, 125, 105891.
- [27] C. Tournassat, M. Bizi, G. Braibant, C. Crouzet, *J. Colloid Interface Sci.* **2011**, 364, 443.
- [28] T. Sato, F. Diallo, *Transport. Res. Rec.* **2010**, 2141, 61.
- [29] H.-B. Yao, Z.-H. Tan, H.-Y. Fang, S.-H. Yu, *Angew. Chem.* **2010**, 49, 10127.
- [30] H. N. M. E. Mahmud, A. Kassim, Z. Zainal, W. M. M. Yunus, *J. Appl. Polym. Sci.* **2006**, 100, 4107.
- [31] D. Liu, P. Yuan, H. Liu, J. Cai, D. Tan, H. He, J. Zhu, T. Chen, *Appl. Clay Sci.* **2013**, 80–81, 407.
- [32] P. Yu, R. J. Kirkpatrick, B. Poe, P. F. Mcmillan, X. Cong, *J. Am. Ceram. Soc.* **1999**, 82, 742.
- [33] A. K. Mishra, S. Allauddin, R. Narayan, T. M. Aminabhavi, K. V. S. N. Raju, *Ceram. Int.* **2012**, 38, 929.
- [34] X. Cong, R. J. Kirkpatrick, *Adv. Cem. Based Mater.* **1996**, 3, 144.
- [35] H. Chen, Y. Yang, D. T. Boyle, Y. K. Jeong, R. Xu, L. S. De Vasconcelos, Z. Huang, H. Wang, H. Wang, W. Huang, H. Li, J. Wang, H. Gu, R. Matsumoto, K. Motohashi, Y. Nakayama, K. Zhao, Y. Cui, *Nat. Energy* **2021**, 6, 790.
- [36] Y. P. Tang, D. R. Paul, T. S. Chung, *J. Membr. Sci.* **2014**, 458, 199.
- [37] J.-X. Zhu, L.-Y. Xu, B.-T. Huang, K.-F. Weng, J.-G. Dai, *Constr. Build. Mater.* **2022**, 342, 127956.
- [38] S. Xia, Z. Wang, H. Chen, W. Fu, J. Wang, Z. Li, L. Jiang, *ACS Nano* **2015**, 9, 2167.
- [39] H. Zhao, Y. Yue, Y. Zhang, L. Li, L. Guo, *Adv. Mater.* **2016**, 28, 2037.
- [40] T. Sumitomo, H. Kakisawa, Y. Owaki, Y. Kagawa, *J. Mater. Res.* **2011**, 23, 1466.
- [41] B. L. Smith, T. E. Schäffer, M. Viani, J. B. Thompson, N. A. Frederick, J. Kindt, A. Belcher, G. D. Stucky, D. E. Morse, P. K. Hansma, *Nature* **1999**, 399, 761.
- [42] F. Barthelat, H. D. Espinosa, *Exp. Mech.* **2007**, 47, 311.
- [43] H. Kakisawa, T. Sumitomo, *Sci. Technol. Adv. Mater.* **2011**, 12, 064710.
- [44] F. Barthelat, H. Tang, P. Zavattieri, C. Li, H. Espinosa, *J. Mech. Phys. Solids* **2007**, 55, 306.
- [45] X. Liu, P. Feng, Y. Cai, X. Yu, C. Yu, Q. Ran, *Chem. Eng. J.* **2022**, 431, 134243.
- [46] X. Liu, P. Feng, X. Yu, J. Huang, *Constr. Build. Mater.* **2022**, 342, 127988.
- [47] X. Liu, P. Feng, X. Yu, X. Shen, G. Geng, B. Lothenbach, *Cem. Concr. Res.* **2022**, 160, 106901.
- [48] S. A. Hamid, Z. Kristallogr. - *Cryst. Mater.* **1981**, 154, 189.
- [49] A. Viani, A. F. Gualtieri, G. Artioli, *Am. Mineral.* **2002**, 87, 966.
- [50] A. P. Thompson, H. M. Aktulga, R. Berger, D. S. Bolintineanu, W. M. Brown, P. S. Crozier, P. J. In 'T Veld, A. Kohlmeyer, S. G. Moore, T. D. Nguyen, R. Shan, M. J. Stevens, J. Tranchida, C. Trott, S. J. Plimpton, *Comput. Phys. Commun.* **2022**, 271, 108171.